ELECTROCHEMISTRY

Effective single web–structured electrode for high membrane electrode assembly performance in polymer electrolyte membrane fuel cell

Yunseong Ji[1,2,3], Ohchan Kwon[1], Ok Sung Jeon[4], Sungdae Yim[2], Yukwon Jeon[5]*, Yong-gun Shul[1]*

To achieve a sustainable society, CO_2 emissions must be reduced and efficiency of energy systems must be enhanced. The polymer electrolyte membrane fuel cell (PEMFC) has zero CO_2 emissions and high effectiveness for various applications. A well-designed membrane electrolyte assembly (MEA) composed of electrode layers of effective materials and structure can alter the performance and durability of PEMFC. We demonstrate an efficient electrode deposition method through a well-designed carbon single web with a porous 3D web structure that can be commercially adopted. To achieve excellent electrochemical properties, active Pt nanoparticles are controlled by a nanoglue effect on a highly graphitized carbon surface. The developed MEA exhibits a notable maximum power density of 1082 mW/cm^2 at 80°C, H_2/air, 50% RH, and 1.8 atm; low cathode loading of 0.1 mg_{Pt}/cm^2; and catalytic performance decays of only 23.18 and 13.42% under commercial-based durability protocols, respectively, thereby achieving all desirables for commercial applications.

INTRODUCTION

Owing to the increasing global energy demand and environmental concerns, the polymer electrolyte membrane fuel cell (PEMFC) is attracting attention as an essential and potential energy conversion device that is environmentally sustainable with no CO_2 emissions. PEMFC is highly efficient for various applications requiring low operating temperature, high energy, and power density, as well as fast start-up ability (*1*, *2*). Commercially, batteries are popular in the eco-friendly transportation field, but their limited driving range and slow charging rate have necessitated the development of the PEMFCs as a more attractive alternative technology (*3*, *4*). However, the main impediments to the expansion of the PEMFC market are the relatively high cost and insufficient durability of the fuel cell stack (*4*, *5*). The main component of a PEMFC is the membrane electrode assembly (MEA) composed of a proton-conducting membrane sandwiched between the catalyst layers (CLs). At the CL, Pt-based catalysts are mainly used; therefore, the Department of Energy (DOE) targeted the Pt loading under 0.10 mg_{Pt}/cm^2 by 2025 to reduce the main cost of electrode layers by increasing the activity and stability of electrocatalysts (*4*–*8*). Moreover, research on the successful implementation of the developed catalyst at the device scale is essential. Therefore, it is important to develop effective electrode materials and fabrication methods, which can be easily applied to the commercial MEA production process for high PEMFC performance and durability; hence, it opens up the upcoming hydrogen economy.

In the PEMFC system, the CL generally consists of carbon supports that have appropriate electrical conductivity and pore structure with high surface area for effective electrochemical reactions. However, carbon can be degraded in a highly corrosive environment under PEMFC operating conditions such as on-off cycling, load cycling, and idling (*9*, *10*). Furthermore, environmental and material factors such as temperature, humidity (*11*), surface functional group (*12*), surface structure (*13*), Pt deposition method (*14*), and operation protocols (*15*–*18*) affect the carbon degradation. The carbon loss not only decreases the electrical conductivity but also substantially diminishes the CL microstructure for the decreased gas transport and enables the exchange of the Pt species with nanoparticles (NPs) via sintering/agglomeration, thereby reducing the electrochemical surface area (ECSA) (*18*–*20*). These problems affect the operation of fuel cells, resulting in low durability, which should be resolved to decrease the life cycle cost. Therefore, the DOE targeted long-term durability for 2025 with the MEA cycling over 8000 hours with a maximum performance loss of ≤20% for automobile applications and catalyst degradation by activity loss and support stability of ≤30 to 40% of the initial mass activity and performance, similar to the New Energy and Industrial Technology Development Organization (NEDO) guideline for durability targets (*7*, *8*, *17*, *21*).

To design an appropriate electrode for efficient PEMFC performance and durability, the structures of the carbon material, surface, and morphology are the critical points that should be considered during CL configuration. First, the carbon materials should have sufficient long-range and ordered graphitic structures with a high degree of graphitization for good electrical conductivity and, particularly, corrosion resistance (*12*, *13*, *19*, *22*, *23*). It is also important to have favorable surface properties for adequate active metal deposition with uniform NP distributions and strong metal support interactions (*23*–*27*). Furthermore, the morphological structure of carbon materials allows an appropriate three-dimensional (3D) configuration of the electrode structure, providing a high surface area and great availability of pores for better reactant/product diffusion. Nanofibrous materials such as carbon nanofiber (CNF) have been studied because of their graphitization, high aspect ratio, connective structures for high conductivity, and favorable pore

[1]Department of Chemical and Biomolecular Engineering, Yonsei University, Yonsei-ro 50, Seodaemun-gu, Seoul 03722, Republic of Korea. [2]Fuel Cell Laboratory, Korea Institute of Energy Research (KIER), Daejeon 34129, Republic of Korea. [3]KIURI Institute, Yonsei University, Seoul 03722, Republic of Korea. [4]Advanced Institute of Convergence Technology, Seoul National University, Suwon 443-270, Republic of Korea. [5]Department of Environmental and Energy Engineering, Yonsei University, 1 Yonsei-gil, Wonju, Gangwon-do 26493, Republic of Korea.
*Corresponding author. Email: ykjeon@yonsei.ac.kr (Y.Jeon); shulyg@yonsei.ac.kr (Y.Shul)

structures (*26*–*30*). In particular, the electrospinning method has been widely used to produce a fine nanofibrous matrix, providing a uniform and controllable web structure (*26*, *27*, *31*–*34*). However, because it is difficult to simultaneously satisfy the requirements of activity and durability, achieving the best balance between the graphitization degree and surface design of carbon supports with a proper morphology can enhance the overall performance of the PEMFC.

Focusing on the fabrication of an optimized CL, various effective methods have been reported to considerably improve the utilization of CLs (*10*, *34*–*37*). For example, CL fabrication methods such as screen printing, inkjet printing, decal transfer, direct coating, spraying, and impregnation are widely used in commercial processes for large-scale preparation of CLs because of their simplicity, low cost, and ease of scalability. However, these methods have several drawbacks that can affect the performance and durability of the CL. In particular, it is difficult to control the thickness, porosity, ionomer distribution, tortuosity, and roughness of the CL and also achieve a highly uniform catalyst distribution due to the random nature of the process, resulting in only 60 to 70% of catalyst utilization (*38*–*42*). On others, chemical vapor deposition and sputter methods provide uniformly stacked CLs by a high degree of control over the thickness, porosity, and roughness of the CL and even multiple types of catalyst materials and surfaces (*35*, *43*, *44*). However, both methods require the accurate control of vacuum and pressure conditions, which is expensive and complex, and therefore, they cannot be easily applied to the commercial scale-up process. Recently, a control of the CL nanostructure is also important to construct a well-organized periodic and uniform porous feature for an improved mass transport, but it is relatively complex, less scalable, and time-consuming to commercialize (*7*, *28*, *45*, *46*).

In this study, an efficient MEA was developed with a thin cathode layer and low Pt-loading to realize a high overall performance by direct electrode deposition using a single nanofibrous CL matrix, which can be applied to real MEA preparation with a simpler process even in a larger scale. The electrospun carbon single web was highly graphitized with high-temperature treatment, and Pt-NPs were uniformly deposited through a nanoglue method to simultaneously achieve high activity and stability. The flexible single-web cathode is directly sandwiched between the commercial anode, membrane, and gas diffusion layer (GDL) for the PEMFC single-cell tests. The developed MEA exhibits excellent performance and durability at various operating conditions.

RESULTS

Graphitized carbon single-web sheet

To obtain a flexible and effective carbon support, a single-web sheet composed of graphitized CNFs was synthesized by electrospinning and high-temperature graphitization processes. Figure 1A illustrates the schematic procedure in the order of electrospinning, stabilization, and graphitization steps. As illustrated by the detailed procedure in fig. S1A, polyacrylonitrile (PAN) nanofibers were electrospun and collected on a spinnable drum (Fig. 1B) under an optimized condition by using 10 wt % PAN/*N*,*N*-dimethylmethanamide (DMF) solution. A wide area of stacked white web sheets was produced, as shown in Fig. 1C, with a uniform average fiber diameter of 200 to 300 nm (Fig. 1D). During the temperature increase at a nonoxidizing condition, a stabilization of the prepared web sheets (Fig. 1E) was followed under an oxidizing atmosphere by the development of a rigid ladder-like structure (fig. S1B) that can prevent mass reduction through the evaporation of volatiles and retain their diameter under the nonoxidizing atmosphere (*47*). Last, a graphitized carbon single web, denoted as gCSW, was obtained after the carbonization procedure (fig. S1B) with dehydrogenation (400° to 600°C) and denitrogenation (600° to 1300°C) steps (*47*). The samples that were annealed at temperatures of 1000°C and very high temperature of 2500°C are denoted as gCSW1000 and gCSW2500, respectively. Notably, flexible and stable gCSW sheets (Fig. 1F) were produced through an optimized condition, which ensured the electrode stability during the fabrication process and could also improve the operation durability.

During the carbonization procedure, it was observed that a perfect CNF fully filled with carbon species was synthesized as from the crosssection illustrated in Fig. 1G. After the final heat treatment, notable reductions in the nanofiber diameters were observed with average values of 132 and 92 nm for gCSW1000 and gCSW2500, respectively. The shrinkage of the fibers at the higher temperature is attributed to the compression of the carbon structure that indicated a higher degree of graphitization. The x-ray diffraction (XRD) results in Fig. 1H confirm this with the carbon peaks at 26.5° corresponding to (002) with a change in d-spacing and crystal size (fig. S2A), showing noticeable crystallization and ordering of the carbon structure for gCSW2500 (*48*).

The highly graphitized structure was further proved in Fig. 2 using various characterization tools. As illustrated in Fig. 2A, a higher degree of graphitization implies that the carbon structure transforms from amorphous to ordered with graphite stacking layers as the annealing temperature increases. Generally, the numerous *c*-axis layer crystallites are nucleated at or below 2200°C, and a further increase in the layer stacking scales only weakly with temperature (*47*, *48*). High-resolution transmission electron microscope (HR-TEM) images in Fig. 2B show visible crystallite fibrils with magnified surfaces. For gCSW1000, the crystallographic ordered structure or parallel stacking was less noticeable. The conversion into a more graphitic structure occurred after heat treatment at the very high temperature of 2500°C, with the development of ribbon-type structured microfibril layers of graphite basal planes (sp^2 type). These ribbon types appeared to pass smoothly from one domain of stacking to the other with ~30 graphite layers (fig. S2A) oriented along the fiber axis during the motion of a highly graphitic structure (*48*, *49*), which is also evident from the Raman and x-ray photoelectron spectroscopy (XPS) analysis.

Figure 2C depicts the Raman spectra with two conspicuous carbon peaks, i.e., vibrational bands: D1-band around 1350 cm^{-1} assigned to amorphous carbon domains and defects of the graphite crystallites and G-band around 1580 cm^{-1} ascribed to the ordered ideal graphitic lattice (*50*). Therefore, the intensity ratio of the *R* value (I_{D1}/I_G) is generally calculated to investigate the degree of graphitization and defects. As expected, *R* values decreased from 5.37 to 0.76 as the annealing temperature increased, indicating the proportion of amorphous carbon that decreased and that of multilayer graphite that increased. Furthermore, the formation of a sharp G2-band at approximately 2700 cm^{-1} for gCSW2500 proves the alternatively repeating ABAB structure stacking of graphene layers (*48*–*50*). Through the deconvolution of each band that is described in detail (fig. S2, B to D), the disappearance of D3 for amorphous carbon and D4 for disordered graphitic lattice supports the

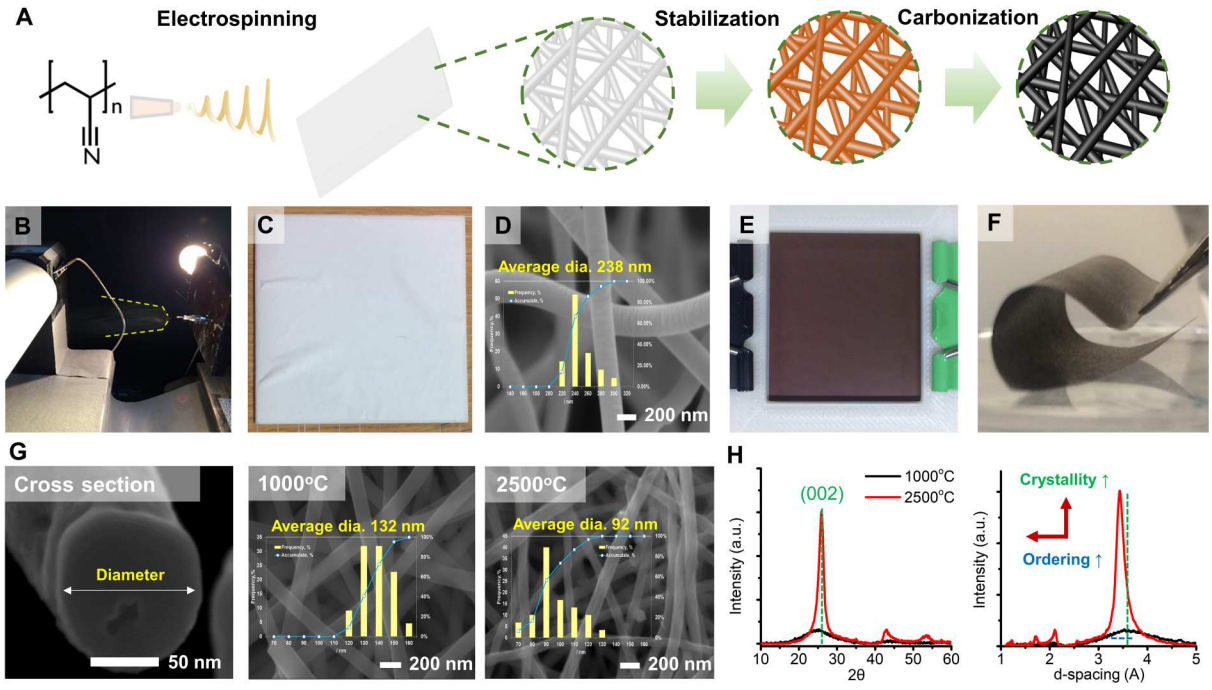

Fig. 1. Synthesis and characterizations of the graphitized single carbon web. (**A**) Schematic illustration of the synthesis of the graphitized single carbon web by the electrospinning method as in the (**B**) photograph. (**C**) Photograph and (**D**) scanning electron microscopy (SEM) image (inset: distribution of the nanofiber diameter) of the electrospun polymer nanofibrous web sheet. Photographs of the (**E**) stabilized and (**F**) carbonized electrospun single carbon web sheet. (**G**) SEM images (inset: distributions of the nanofiber diameters) and (**H**) XRD patterns by 2θ and d-spacing for the graphitized single CNFs treated at 1000° and 2500°C.

increased degree of graphitization with a well-defined structure (*47*–*50*). This kind of reorientation of surface structure can enhance the surface alignment–electrode layer for better durability (*13*).

Figure 2D and fig. S3 show the change in the chemical composition and structure that was investigated by the XPS analysis. During the synthesis of gCSW, as shown in fig. S3A, the proportion of carbon increases, whereas those of O, N, and even H decreases through dehydrogenation and denitrogenation, which is consistent with the elementary analysis. Figure 2D demonstrates the XPS peaks of C 1s for gCSW1000 and gCSW2500 with the assigned chemical bonding, and each peak was deconvoluted, as summarized in fig. S3 (B to D), to evaluate the chemical structural changes. Referring to the peak at 284.2 eV for the C─C bond of sp^2-bonded carbon, the intensity on the gCSW2500 notably increased with a compositional portion of almost 100%, while the relatively lower intensity of the C─C peak for gCSW1000 and additional peaks of carbon bonds (C─N and C─O) were exposed. As is clear from these results, gCSW2500 represents the formation of a highly carbonized and graphitized structure; however, it is clear that the surface functional groups barely remained after the reduction of O and N species; this may cause problems with Pt NP deposition and control.

Synthesis of Pt/PCA/gCSW2500

Figure 3 depicts the synthesis procedure and results for the Pt deposition on gCSWs through the nanoglue method using 1-pyrene carboxylic acid (PCA). As illustrated in Fig. 3A, the process of Pt deposition was conducted beginning with PCA coating and followed by microwave polyol methods to distribute uniformly small Pt NPs on the gCSW supports. The strong bonding and distribution issues of the Pt NPs on the surface are very important, as it is related to agglomeration, resulting in the rapid decline of catalytic activity. However, CNFs, similar to our gCSWs in which less or no surface functional groups remained, generally have 2D crystals or bundles and intrinsic hydrophobic surfaces, which make Pt-NPs difficult to disperse in polar solvents.

To improve the Pt-NP dispersion and bonding, PCA is used as an amphiphilic functional agent, where aromatic hydrocarbons with hexagonal carbon rings pi-functionalized the CNF surface. Figure S4A illustrates a nondestructive PCA coating method that includes dipping the prepared gCSW2500 in water/alcohol + PCA solution to retain the nanofibrous web structure. Moreover, as observed from the confocal microscopy and scanning electron microscopy (SEM)–energy-dispersive x-ray spectroscopy (EDX) analysis (fig. S4, B and C), PCA was finely coated on the gCSW2500 through a noncovalent π-π interaction (pi-functionalization). The pyrene part (lyophilic portion) of the molecule sticks to the carbon structure, which is the bonding part with Pt species (*48*–*50*). Simultaneously, the hydrophilic COOH part remains stably suspended in an aqueous medium owing to the enhanced wettability of solvents. This is verified, as shown in fig. S4D, by the relatively low water contact angle of 53° for the PCA-coated gCSW2500. At the water/hexane (1:1) in fig. S4E, the dispersion of PCA/gCSW2500 in the water layer rather than the hexane layer indicates the water affinity due to the carboxylic acid functional groups, which is also found in the water and ethanol solvents. Consequently, a key advantage of producing gCSW in this manner is that it is possible to strongly distribute the Pt NPs on the carbon surface.

A Pt-NP deposition step (Fig. 3A) through the polyol method was performed to adequately control the sizes, shapes, compositions, and crystallinity with a heating homogeneity with microwave

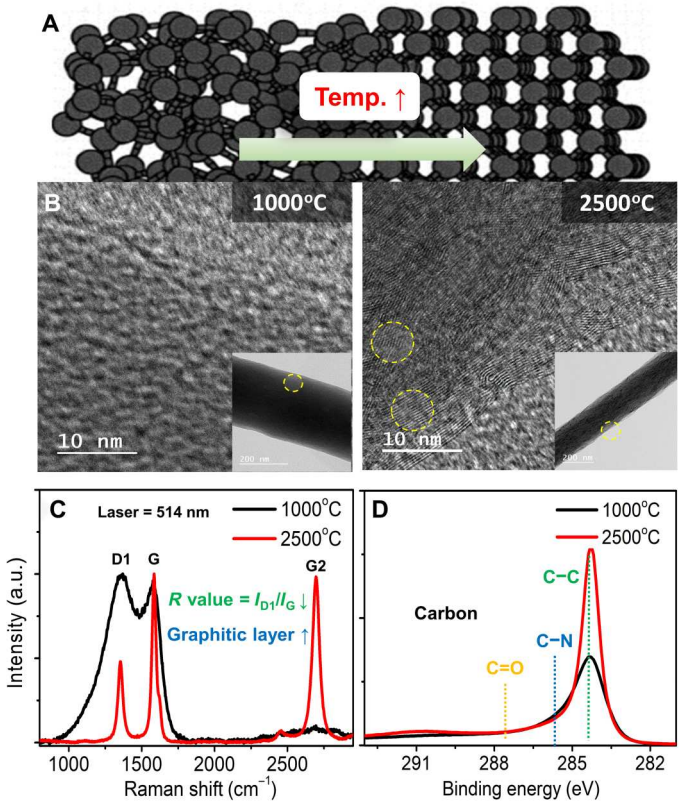

Fig. 2. Structural changes by different treatment temperatures. (**A**) The illustration of the graphitization process and (**B**) TEM images (insets: morphologies of the CNFs), as well as the (**C**) Raman and (**D**) XPS C 1s analysis for the graphitized single carbon nanofibrous webs treated at 1000° and 2500°C.

assistance (*26*, *27*, *51*). As shown in fig. S5A, the prepared PCA/gCSW2500 was dipped in ethylene glycol (EG) with the Pt precursor (40%) and then microwaved. The wettability of EG was sufficient to execute this method with great dispersion (fig. S5B). As illustrated in fig. S5A, the Pt species is expected to attach to each PCA functional group and then reduce as nanoglued Pt NPs on the surface of PCA/gCSW2500 with highly uniform distribution. Figure 3B demonstrates the TEM-EDX analysis that displays excellent distribution of Pt species entirely on the gCSW support. From the XRD analysis (fig. S5C), major diffraction peaks of Pt metal were detected well at 39.4° (111) and 46.2° (200) (JCPDS card no. 04-0802) for all samples after the Pt deposition process. The major peak for the Pt/PCA/gCSW2500 was slightly broader than the other, indicating better distribution of small NPs. From the size calculation through Scherrer's equation, Pt NPs exhibited a range of 3 to 5 nm, which is commonly known as an appropriate size for a good oxygen reduction reaction (ORR) activity (*52*–*56*). The consistent sizes were confirmed by the HR-TEM analysis. In Fig. 3C, it can be observed that the Pt NPs are well deposited on all gCSW surfaces, while a partial agglomeration of the Pt species on the 2500°C-treated gCSW was observed possibly because of the less number of surface functional groups, as confirmed. However, the PCA-coated gCSW2500 shows excellent Pt-NP distribution on the entire carbon surface with a uniform shape of a spherical morphology, which is close to the Pt NPs at the commercial Pt/C (fig. S5D). Furthermore, from the NP size distribution analysis, shown in Fig. 3D, Pt NPs at Pt/PCA/gCSW2500 are even smaller, with an average size of 2.8 nm than the other samples (average of 3 to 5 nm) with a relatively shaper peak, thereby proving excellent uniformity.

The results of the XPS analysis support the nanoglue effect between Pt and gCSW with high distribution. Figure 3E displays the typical XPS Pt 4f spectra of Pt/PCA/gCSW2500 for metallic Pt on the carbon supports with mainly Pt^0. However, it also contains relatively higher portions of Pt^{2+} and Pt^{4+} owing to the strong bonding with the functionalized carbon surface, compared to the other samples (fig. S6A). Because it is important to have a strong bonding structure of Pt and support, the degree of the functionalized surface can be confirmed by the deconvoluted C 1s and O 1s XPS spectra. It was observed that the C species of C—O and C═O (fig. S6B) increased at Pt/PCA/gCSW2500, and the O content (fig. S6C) also increased. This indicates the presence of a higher amount of functional groups at the surface after PCA coating than the original gCSW2500 produced, which is strongly bonded with the increased Pt ionic species. Consequently, it shows a nanoglue effect that can enhance not only the catalytic activity through the well-distributed small Pt NPs but also the durability at the PEMFC operating conditions through the strong Pt and support interactions.

Electrochemical characterizations

As shown in Fig. 4, the prepared catalysts with similar Pt loading were examined to evaluate the half-cell activity and durability using a three-electrode system. Cyclic voltammetry (CV) and linear-sweep voltammetry (LSV) measurements were conducted to confirm the ORR activity and durability before and after a potential cycling test (PCT). To begin with the CV curves in Fig. 4A, the current shown at a particular potential window indicates the magnitude of a specific reaction. All catalysts exhibited well-developed H_2 adsorption/desorption at lower 0.4 V and O_2 adsorption/desorption peaks at upper 0.6 V without additional reactions. Comparing the H_2 desorption region, the area for Pt/PCA/gCSW2500 was observed to be larger than the other noncoated regions and comparable with the Pt/C. Therefore, higher ORR activity and its trend can be also confirmed by the LSV results, as shown in Fig. 4B. Similar to the CV results, the onset potential, one of the indicators for ORR activity in LSV, was notably shifted toward positive potentials from 0.96 to 0.99 V after PCA coating, resulting in the same value with Pt/C. The limiting current densities of the CSWs were higher with an average value of 5.3 mA/cm^2 (Pt/C: 4.7 mA/cm^2) owing to a greater mass transfer effect by the nanofibrous web structure.

To clearly compare the catalytic durability, Fig. 4C shows the values of ECSA, mass activity, half-wave potential, and specific activity, along with the decay rates during the PCT for 6000 cycles (figs. S7 and S8). The PCT protocol is designed to have equivalent to or even more severe operating conditions than the DOE durability test protocol to evaluate a rapid carbon corrosion in a potential range of 1.0 to 1.6 V (*15*). From the CVs in Fig. 4A, the ECSA values for the number of active sites on the electrocatalysts are calculated by the total charge amount at the H_2 desorption peak using the equation, ECSA = $Q_H/m \cdot q_H$. Here, Q_H is the charge for H_2 desorption by peak integration with the baseline from the double layer, m is the amount of metal loading, and q_H is 210 mC/cm^2, i.e., the charge required for the monolayer adsorption of H_2 on Pt surfaces. As expected, the specific ECSA value for the developed Pt/PCA/gCSW2500 revealed a reasonable value of 32.76 m^2/g, comparable

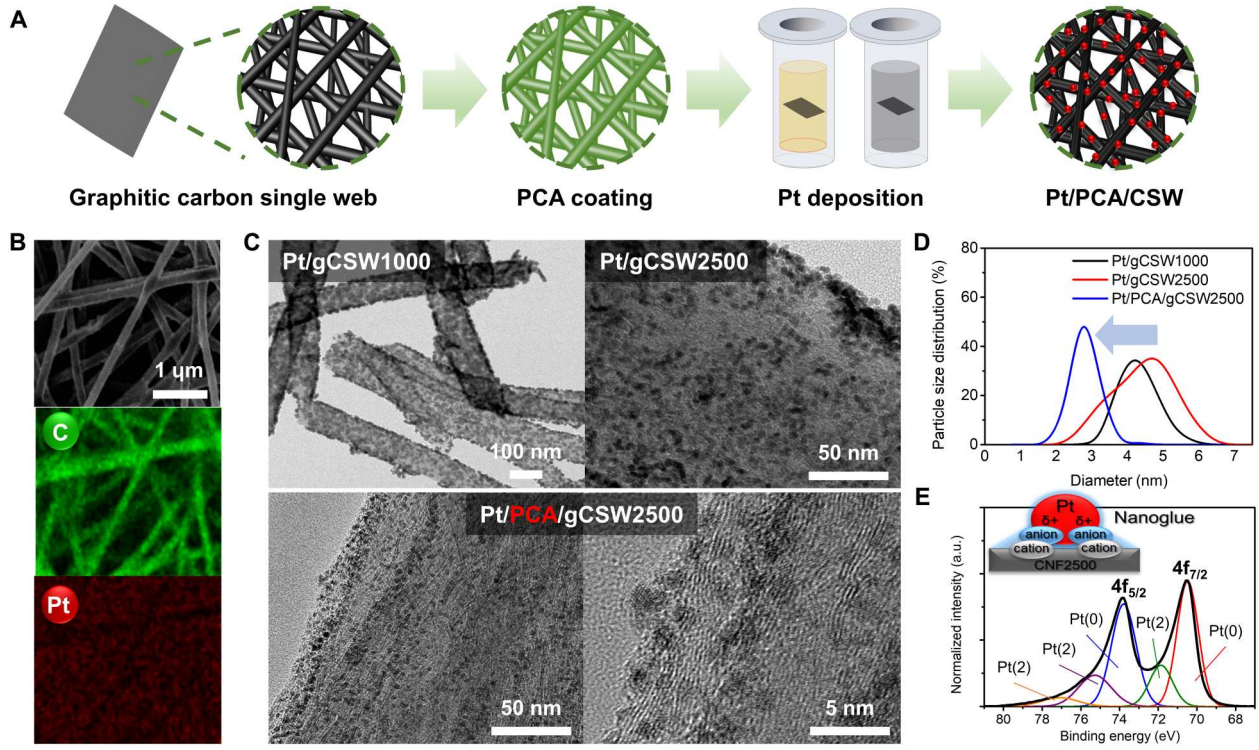

Fig. 3. Synthesis and characterization of the platinum (Pt) NP distribution on the graphitized single carbon nanofibrous web. (**A**) Schematic illustration of the Pt NP distribution process on the graphitized single carbon nanofibrous web through the PCA coating deposition method. (**B**) SEM images with EDS mapping images of C and Pt elements for the Pt/PCA/gCSW2500. (**C**) TEM images with the (**D**) NP size distribution for the samples of Pt/gCSW1000, Pt/gCSW2500, and Pt/PCA/gCSW2500 and (**E**) XPS Pt 4f analysis for the Pt/PCA/gCSW2500 (inset: expected Pt deposition structure through a nanoglue effect by the PCA coating).

to Pt/C (table S1). This is remarkably enhanced by the PCA coating owing to the improved distribution of small Pt NPs, thereby causing a difference in the initial exposed surface area. The interparticle distance and coarsening at the nanowire structure may also have a positive effect on the surface state to enhance the Pt utilization (*55*–*57*). During the PCTs, carbon supports generally experience electrochemical corrosion and degradation owing to a decrease in the number of exposed active sites (*15*). In the CV curves after PCTs for 6000 cycles (fig. S7), the signature peak locations remained similar, but the peak intensity and area changed according to the degree of degradation. It is clear that Pt/C shows a diminished shape of the initial CV with ECSA decay rate of 57.39% (Fig. 4D). Unexpectedly, Pt/PCA/gCSW2500 exhibited not only comparable activity but also exceptional durability with a decay rate of only 5.59%, which can be attributed to the corrosion resistivity of the highly graphitized carbon nature (*12*, *13*).

Half-wave potential, mass, and specific activity can be calculated from the LSV polarization curves shown in Fig. 4B to express the activation energy of electrocatalysts as the overpotential and magnitude of a reaction as a form of current density. With a similar tendency with CV in fig. S8, we observed that the half-wave potentials shifted after PCTs from their initial values. A notable decay was observed in Pt/C, which are mainly amorphous carbons, whereas the highly graphitized samples of Pt/gCSW1000, Pt/gCSW2500, and Pt/PCA/gCSW2500 were relatively stable with a decay rate of under 5%. Furthermore, mass activity was calculated from the current density per unit mass taken at 0.90 V by approximately 0.1 A/mg, which is commonly reported for the Pt on carbon electrocatalysts (*52*, *54*). Using the mass activity and ECSA values, it is also possible to calculate the specific activity, which is the activity per quantity of Pt (mA/cm^2_{Pt}), to evaluate a physical property of Pt NPs (*7*, *52*, *54*). As we confirmed that the PCA coating improves the Pt NP′s physicochemical control, Pt/PCA/gCSW2500 shows outstanding values of both mass and specific activities for 154.98 mA/mg and 473.02 mA/cm^2_{Pt}, respectively, than the noncoated samples and Pt/C catalyst (155.60 mA/mg and 275.78 mA/cm^2_{Pt}, respectively) with a similar mass activity and almost twice the specific activity. Notably, Pt/PCA/gCSW2500 exhibits excellent durability with decay rates of 10.75 and 6.79% of mass and specific activities, respectively, compared to Pt/C (83.84 and 62.07%). In fig. S9, the HR-TEM images illustrate the change in the size and distribution of Pt NPs after the durability tests. As expected, Pt NPs at the Pt/C were highly agglomerated after PCT with substantial degradation. However, the highly graphitized catalysts show almost no change in their morphology due to the nanoglue effect that not only affects the great catalytic activity but also alleviates the Pt dissolution and growth (*12*, *55*–*58*). As our accelerated test conditions are equivalent to or even harsher than the DOE and NEDO protocols (*14*), the PCT results for Pt/PCA/gCSW2500 satisfy the technical targets of DOE 2025 and even NEDO, catalytic activity <40% after 6000 cycles, which is effective for the long-life operation of PEMFC (*7*, *15*, *17*, *21*, *35*).

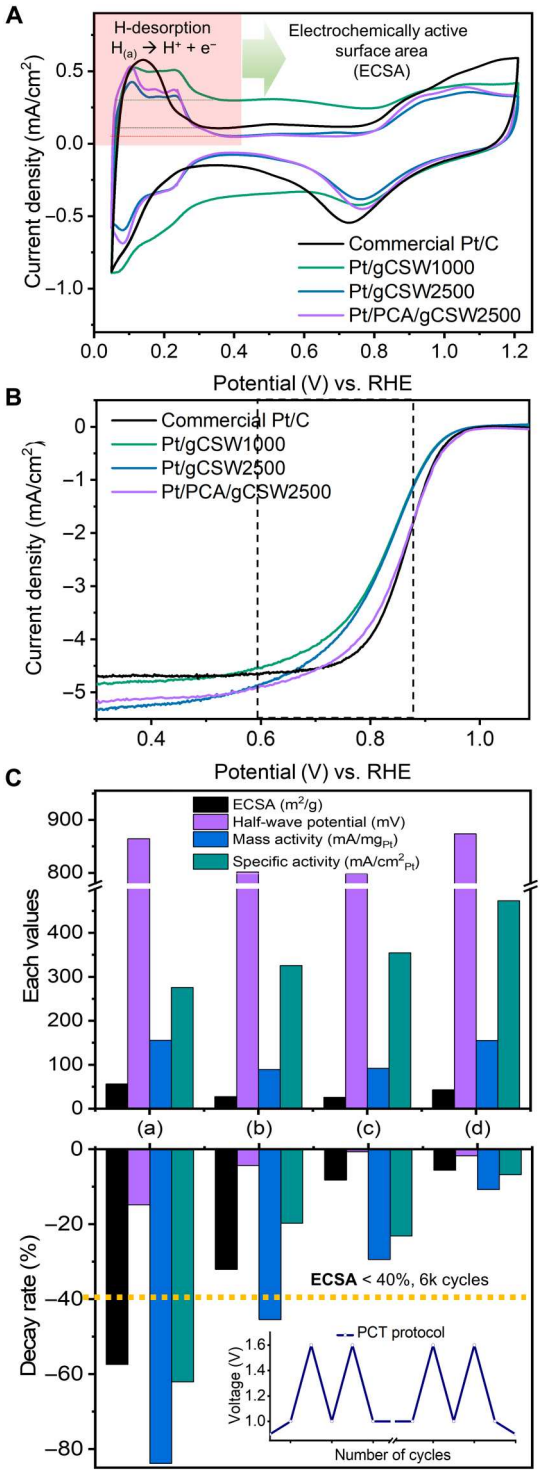

Fig. 4. Half-cell performance of the Pt/PCA/gCSW2500. (**A**) CV and (**B**) polarization curve in 0.5 M H_2SO_4 with (**C**) comparison of the half-cell initial performances on ECSA, mass activity, half-wave potential, and specific activity, as well as these decay rates (table S1) during the durability tests for 6000 cycles based on the PCT protocol (inset), for (a) commercial Pt/C, (b) Pt/gCSW1000, (c) Pt/gCSW2500, and (d) Pt/PCA/gCSW2500.

Preparation of MEAs with single-web cathode

The developed Pt/PCA/gCSW2500 was evaluated in as a cathode material for a single-cell PEMFC (Fig. 5) to investigate the proven electrochemical property from the half-cell results. Figure 5A demonstrates the fabrication process of the MEA using the single nanofibrous sheet using a direct hot-pressed deposition method. As shown in fig. S10 (A to E), Pt/PCA/gCSW2500 was prepared with two different sizes of 1 cm by 1 cm and 2.5 cm by 2.5 cm with low Pt cathode loading of 0.1 mg/cm^2. To apply to a single cell, the electrode was directly hot-pressed onto the other side of the anode-coated membrane. For comparison, Pt/gCSW2500 and particulate Pt/C with the ionomer mixture were sprayed (fig. S11, A and B). Subsequently, GDLs were attached to both sides, and single cells were assembled by a unit cell system for PEMFC performance tests (fig. S10F). The proposed MEA preparation was possible owing to the flexibility of our single web, showing great potential for the next-generation MEA fabrication by the simple deposition of the electrode layers; hence, it is efficient to apply to the commercial scale-up process.

Figure 5B displays a perfect nanofibrous cathode structure by Pt/PCA/gCSW2500, which is finely stacked and attached to the membrane surface. From the SEM cross-sectional images in fig. S12 (A to C), it can be observed that three distinctive layers fabricated with Pt/PCA/gCSW2500, membrane, and Pt/C had thicknesses of 5, 20, and 1.8 μm, respectively. The chemical composition of the Pt/PCA/gCSW2500 cathode layer was confirmed by the energy dispersive X-ray spectroscopy (EDS) mappings, as shown in Fig. 5C, showing well the distribution of all elements, especially Pt, which is also observed for the non–PCA-coated Pt/gCSW2500 cathode layer (fig. S12C). As shown in the table in fig. S12D, a desired ratio of Pt, carbon with PCA, and ionomer was achieved for both cathode layers with only a difference in the amount of O due to the absence of PCA. On the basis of these images, the characteristics of CNFs were evidently observed; CNFs could be the electrical channel in the MEA for an effective electron transfer in the electrode. Furthermore, the gCSW analyzed by FIB-SEM (fig. S12E) exhibits a distinctive pore structure and connectivity compared to the particular Pt/C-based cathode layer (fig. S11, C and D). The thickness of the cathode layer was also approximately two to three times greater than the Pt/C-based layer, owing to the higher volume of the nanofibrous feature. Figure 5D illustrates that the nanofibrous structured electrode has much higher pore volume than the particular electrode with relatively larger pore size ranges. This is a key point for a short mass transfer in the electrode, where gCSW could offer enhanced mass transfer and effective electron/ionomer transport from a connected pathway (*28*–*34*), consequently providing higher MEA performance and even durability for efficient PEMFC usage.

PEMFC single-cell application

To confirm the practical performance and durability of the MEAs with a Pt/PCA/gCSW2500 cathode, several electrochemical analyses were performed at a single-cell system. As expected in Fig. 6A, the nanofibrous cathode could offer a specific path for mass transfer from the large pores to the interior of the electrode (Fig. 5) and high conductivity from the straightforward pathway across the electrode, which provides a more effective transport property than the particle-based MEA by commercial Pt/C, as shown in Fig. 6B. All the single-cell tests were conducted at the same practical operating

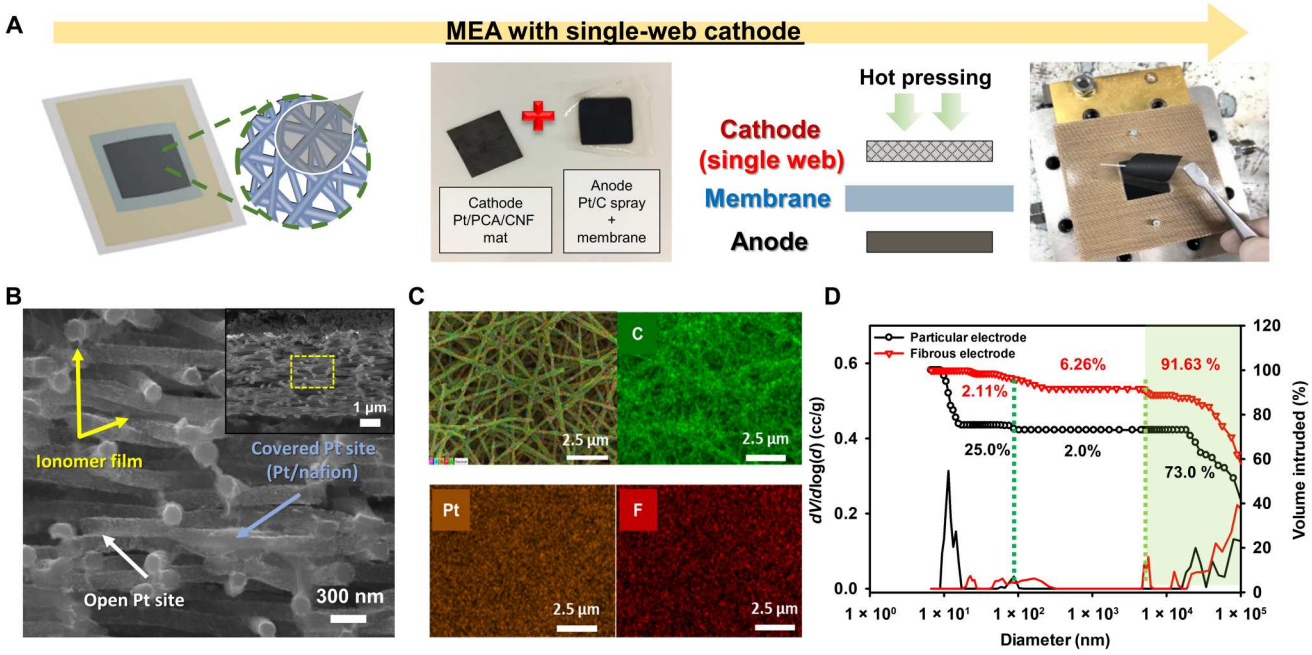

Fig. 5. A single-web MEA for the PEMFC application. (**A**) Schematic illustration of the preparation of a single-web MEA with Pt/PCA/gCSW2500. (**B**) Cross section of the magnified SEM image (inset: SEM image of the whole MEA). (**C**) EDS mapping images of C, Pt, and F elements for the Pt/PCA/gCSW2500-based nanofibrous cathode layer. (**D**) Pore size and volume distribution analysis with a comparison of the particular and nanofibrous single-web electrodes.

conditions of 80°C, 50% relative humidity (RH), H_2/Air, and 1.8 atm. The initial *I-V* performances of the representative MEAs are shown in Fig. 6C. As expected from the half-cell measurements, the Pt/PCA/gCSW2500 nanofibrous cathode achieved better performance than the Pt/gCSW2500 and Pt/C-based cathodes. A more comprehensive analysis of the results shows that the *I-V* curve can be divided into three zones according to the critical reason for overpotentials (*59*). In the kinetic zone at open-circuit voltage (OCV) to 0.75 V, the activation overpotential is usually determined by the catalytic ORR activity. The OCVs were similar to the value in the range of 0.99 to 0.97 V, owing to the similar catalytic activity and adequate electrical conductivity due to the well-connected CNFs, which delivered suitable electrical pathways to reduce the resistance of the cathode layer with an increased number of triple boundary phases. However, a difference in performance is observed, i.e., better catalytic activity for the developed cathodes, which can also be confirmed by the CV analysis. Figure 6D shows the advanced intensity of the H_2 desorption peak with a relatively higher ECSA value than the Pt/C, which is consistent with the half-cell results (Fig. 4). At 0.40 to 0.20 V, the mass transfer–controlled zone indicates the effectiveness of transportation where a diffusion limitation occurred because of the lack of O_2 reactant on the Pt surface (*59*). Therefore, the huge performance difference in this zone for the Pt/PCA/gCSW2500 cathode is understandable, as the nanofibrous web structure provides a high surface area and a 3D open pore configuration with better mass transfer at the electrode. According to the impedance analysis shown in Fig. 6E, it is also confirmed that a smaller mass transport loss occurred at 0.6 V than Pt/C, while the ohmic and activation losses were smaller than those of the Pt/gCSW2500 cathode.

In summary, the excellent performance of the Pt/PCA/gCSW2500 cathode in the ohmic polarization zone of 0.75 to 0.40 V can be attributed to the combination of both properties at the kinetic and mass-transfer zones. While Pt/gCSW2500 and Pt/C-based cathodes exhibited power densities of 750 and 923 mW/cm^2 (0.2 mg$_{Pt}$/cm^2), respectively, Pt/PCA/gCSW2500 revealed an excellent performance of 1668 mA/cm^2 at 0.6 V with a maximum power density of 1082 mW/cm^2 with a low cathode Pt loading of 0.1 mg$_{Pt}$/cm^2. As shown in Fig. 6F, the excellent performance of Pt/PCA/gCSW2500 cathode was achieved at a large-sized MEA (2.5 cm by 2.5 cm), with only a minimal loss in the mass transport property, indicating its applicability to mass production of the effective wide MEAs for PEMFC commercialization.

Because the durability issue is also a crucial point to consider for realizing a marketable PEMFC, Fig. 7 demonstrates the single-cell investigations for corrosion resistivity using two different protocols based on DOE and NEDO, respectively, with the cycling condition of 1.0 to 1.5 V and a scan rate of 500 mV/s at 80°C, RH100. *I-V*, impedance, and CV measurements were conducted before and after the operation cycles. The operating conditions were fixed as those of basic single-cell tests. The carbon corrosion was induced on the basis of the potential cycling condition of 1.0 to 1.5 V and a scan rate of 500 mV/s at 80°C and RH100. Figure 7A shows the *I-V* curves for the MEAs with commercial Pt/C and Pt/PCA/gCSW2500. Both the MEAs started with a similar performance at a low loading of 0.1 mgPt/cm^2 for Pt/PCA/gCSW2500 (Pt/C = 0.2 mg$_{Pt}$/cm^2). Impressively, the performance of this MEA remained constant for over 10,000 cycles with stable high-frequency resistance (HFR) and charge-transfer resistance regions (fig. S13). Although a slight decrease in stability was observed after 20,000 cycles, it is still acceptable when compared to a commercial MEA. The Pt/C-based MEA showed a remarkable decline in performance and large

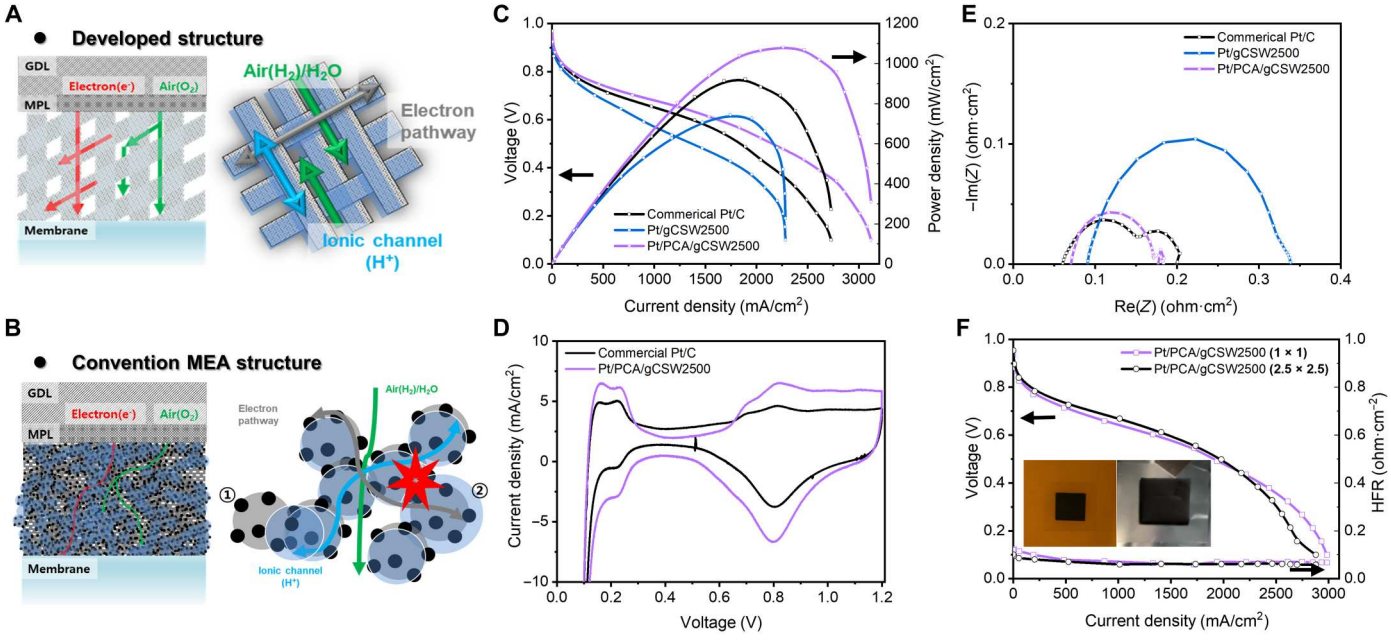

Fig. 6. PEMFC performances. Illustrations of the expected electrochemical reaction mechanisms at the (**A**) nanofibrous single-web MEA and (**B**) conventional particular MEA. Single-cell tests through (**C**) *I-V-W* plots, (**D**) CV, and (**E**) impedance (0.6 V) analysis for the MEAs composed of commercial Pt/C, Pt/gCSW2500, and Pt/PCA/gCSW2500, respectively. (**F**) PEMFC performances of the Pt/PCA/gCSW2500-based MEAs with different active area size of 1 × 1 and 2.5 × 2.5 (inset: photos of the prepared MEAs). All single-cell tests are performed at T_{cell} = 80°C, 50% RH, H_2/air, and 1.8 absolute (1 atm + 0.8 gauge).

increase in resistances of HFR and charge transfer, simultaneously, after only 2000 cycles (fig. S14). This may be because carbon black can be easily oxidized into CO_2 owing to its defect sites, as well as loss of its active sites and conducting pathways for electrons and ions. In other words, the highly graphitized gCSW2500 is more stable because of the defect-free surface (*12*–*15*, *60*).

The evaluation of single-cell durability was conducted by CVs in terms of the change in active Pt sites after each corrosion test. The normalized ECSAs, according to the number of cycles by each protocol, are shown in Fig. 7 (B and C). The initial values were different owing to the different ranges and applied methods to obtain the CV curves. Similar ECSA values of Pt/C and Pt/PCA/gCSW2500 were observed for each system. As has been established in previous studies, Pt/C showed notable degradation at the point of 500 cycles when potential cycling was applied, which can be easily observed in carbon corrosion protocols with considerable changes in ECSA values. Subsequently, after only 2000 cycles by both durability tests, approximately 50% of the initial values in the ECSA resulted in decays of 41.76 and 48.01% for DOE and NEDO protocols, respectively (table S2). Distinctively, the MEA with Pt/PCA/gCSW2500 was considerably stable at the initial points until 10,000 cycles owing to the stable graphitic wall formed along the surface and the structural effect of the 1D structured carbon support. The ECSA value attenuated slowly at a constant rate up to 20,000 cycles, with mere decays of 23.18 and 13.42% for DOE and NEDO protocols, respectively (table S3). Furthermore, these results enormously overcame the DOE target 2025 of catalyst degradation with activity loss and support stability by ≤30 to 0% of the initial values, maintaining the number of active sites with minimal change. As expected, the active Pt NP sizes at Pt/PCA/gCSW 2500 were also stably preserved for 20,000 cycles owing to the PCA nanoglue effect, whereas growth in size was considerably observed at Pt/C (tables S2 and S3). On the basis of these results, it can be inferred that the large difference in durability originated from the high graphitization of the support and preservation of the Pt morphology.

Summarizing the performances in Fig. 8, our developed MEA with the Pt/PCA/gCSW2500 cathode demonstrates better half-cell catalytic, especially specific activity compared to those of other recent works using commercial Pt/C based catalysts, which, additionally, appears to improve the mass activity using a Pt interdistance control (*55*, *56*). Our MEA with direct CL deposition can be conveyed to the high MEA performance at considerably low Pt loading and similar conditions, which may be more effective than the decal and spray used Pt/C-based MEAs. With a substantially better durability at both rotating disk electrode (RDE) and MEA measurements compared to other carbon-based electrodes from the latest literature, the developed MEA with the Pt/PCA/gCSW2500 cathode not only has the advantages of an efficient fabrication method but also results in an exceptional PEMFC performance and durability.

DISCUSSION

The current work reported a simple electrode fabrication method via direct CL deposition using a well-designed carbon single web that results in excellent PEMFC performance and durability. The carbon single web was prepared by electrospinning to secure the macropores to facilitate the transfer properties. While maintaining this structure, the carbonaceous source was graphitized by thermal treatment with annealing growth until 2500°C, and the size and interspace of carbon were modified into a ribbon-type graphitic

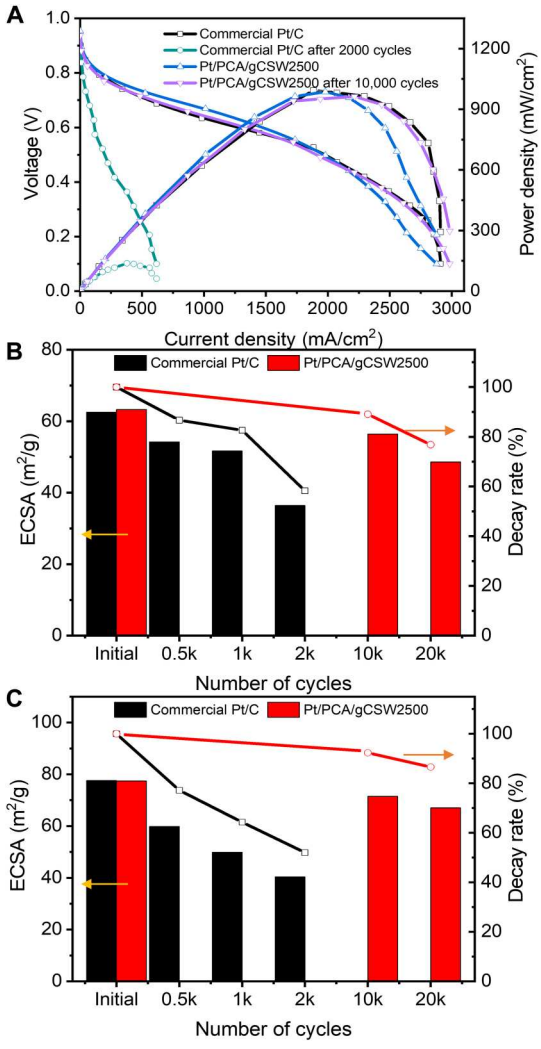

Fig. 7. PEMFC durability tests by two different protocols. Single-cell durability tests of the MEAs composed of commercial Pt/C and single-web Pt/PCA/gCSW2500, with the results of (**A**) *I-V* performance plots before and after the DOE protocol (T_{cell} = 80°C, 50% RH, H_2/air, and 1.8 atm), as well as ECSA values and its decay rates (summarized from tables S2 and S3) under (**B**) DOE and (**C**) NEDO protocols, respectively, at every 500, 1000, 2000, 10,000, and 20,000 cycles.

structure notably different compared to that at 1000°C, resulting in excellent carbon corrosion resistivity. The carbon single-web electrode can suppress surface pores for maximizing Pt utilization through the control of Pt at easily accessible locations for higher catalytic activity, which is additionally improved by the nanoglue effect from PCA coating. The developed Pt/PCA/gCSW2500 was easily deposited by a direct hot press on the membrane; this can improve the commercial MEA production process with a simpler process even in a larger scale. The developed MEA exhibited superior performance and durability, realizing the commercial DOE and NEDO targets at low Pt loading and practical operating conditions. Although there are uncertainties in stack performance and mass production, we can attempt to replace the commercial MEA with a CL structure and fabrication method to facilitate further expansion of the PEMFC market.

MATERIALS AND METHODS

Electrospun PAN nanofibrous web sheet

A nanofibrous web sheet was synthesized through the electrospinning method using a spinnable PAN solution. The polymer solution was made by dissolving PAN powder (M_w= 150,000 g/mol) in DMF with a proportion by weight to obtain solutions of the concentrations of 10 wt % PAN. The solutions were stirred for 1 day to attain complete dissolution and mixing for a clear-colored homogeneous state, although this duration could be reduced by heating the solution at 70°C. When the solution was heated, as-prepared solutions were cooled to room temperature before electrospinning. The experimental setup of an electrospinning process was set up in a chamber with controlled conditions of 20°C and 30% RH. The prepared solution was placed in a plastic syringe and flowed into a 30-gauge nozzle tip (inner diameter, 0.15 mm). The feed rate of the solution was maintained using a syringe pump (KD Scientific) and the voltage supplied from a power supply to the needle. The voltage and distance were kept constant at 18 kV and 15 cm, respectively, with the rate of 200 μl/hour, which produced minimum diameter fibers of approximately 250 nm. The electrospun fibers were collected above the earthed rotating Al drum.

Graphitic carbon single-web sheets

The graphitized CNFs were prepared with a procedure of stabilization (oxidization), carbonization, and graphitization steps, as summarized in fig. S1 (*47*). First, a box-type furnace was used to convert electrospun nanofibers at the web sheet into stabilized CNFs in a cubicle by heating at a ramp rate of 1°C/min to 270°C and retained for an hour under an air atmosphere (*61*). Then, the stabilized nanofibrous web sheet was annealed in a high-temperature graphite furnace (TNS vacuum) at the temperatures of 1000° and 2500°C with a fixed treatment condition of ramp rate at 5°C/min and 3-hour plateau time to produce single-carbon nanofibrous web sheets with a different order of graphitization. The matrix thickness was controlled to around 4 to 5 μm. For convenience, the heat-treated carbon single-web sheets were named following the final heat temperature, for example, gCSW1000 and gCSW2500.

PCA functionalization on CSW2500

A nondestructive platinum (Pt) deposition method was used to finely load Pt NPs on the selected graphitized CSW2500 using a modified PCA (Sigma-Aldrich) coating method (fig. S4). To functionalize the graphitized carbon surface, a noncovalent functionalization method using PCA coating was applied. PCA (0.05 g) was completely dissolved in 200 ml of ethanol by sonicating for 10 min. CSW2500 (0.5 g) was added to the solution for 10 wt % PCA adsorption on the surface, and 50 ml of deionized (DI) water was added. The mixture was stirred for 3 hours, and then, filtration/washing by water/ethanol was repeated. The treated sample, named as PCA/CSW2500, was vacuum-dried at 70°C overnight.

Pt deposition on PCA/gCSW2500

For the Pt deposition on the carbon surfaces, a microwave polyol process was used. A desired amount (Pt = 40 wt %) of chloroplatinic acid hexahydrate ($H_2PtCl_6{\cdot}6H_2O$, Kojima Chemicals) was dissolved in 50 ml of EG (Sigma-Aldrich) under vigorous stirring for 30 min. NaOH (1 M; Sigma-Aldrich) was introduced to adjust the pH of the solution to 11 and precisely controlled because the pH is one of the

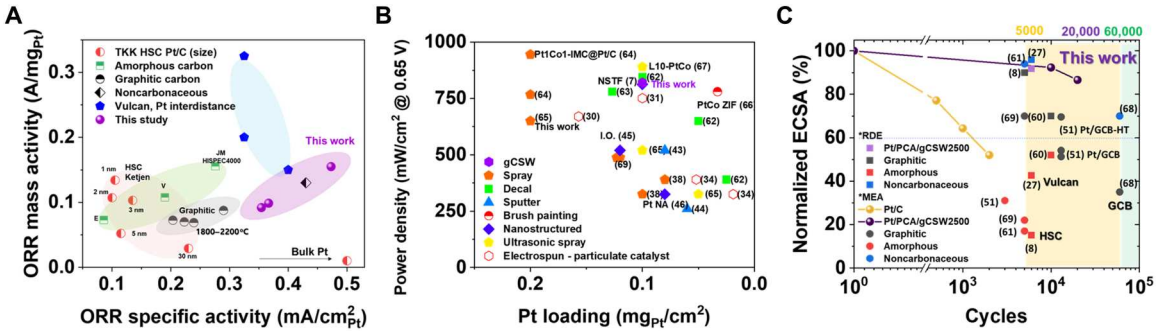

Fig. 8. Performance summary. Comparisons with recent works on the (**A**) half-cell performance of the mass and specific activities at H_2SO_4 solution (*52*, *54*, *55*, *60*, *62*) and the (**B**) MEA performance of the power density (at 0.65 V) and Pt loading at similar conditions (*7*, *30*, *31*, *34*, *38*, *39*, *43*, *44*, *46*, *62*–*68*). (**C**) Durability comparisons of the half cell and MEA test results with latest works (*8*, *27*, *51*, *62*, *69*, *70*).

critical operating parameters. Then, an appropriate amount of the prepared PCA/gCSW2500 support was added to the solution to produce an electrode material, 40 wt % of Pt. The resulting suspension was stirred for 1 hour at room temperature, then poured in a Teflon vessel, and placed in a microwave oven. Microwave reaction was performed at 160°C for 90 s. As a consequence of the microwave-assisted polyol method, the Pt precursor was reduced to a metallic state as Pt NPs on the support material. Last, a sample was achieved after filtration, washing, and drying processes for 8 hours at 80°C vacuum oven. The synthesized Pt NP–loaded single-carbon nanofibrous web sheet was named as Pt/PCA/gCSW2500. For comparison, Pt NPs were loaded on the prepared CNF samples without PCA functionalization. The same method as above was used, and the samples are denoted as Pt/gCSW1000 and Pt/gCSW2500.

Characterizations

The morphological characterization of synthesized materials was observed using FE-SEM (JEOL-7800F, JEOL) to obtain the morphological appearance of the as-spun/treated nanofibers and web sheets. Then, to determine the average nanofiber diameters and distributions, an image processing program, Image Pro, was used. For each sample, approximately 300 readings for the nanofiber diameters were recorded, and statistical analysis was carried out by constructing a histogram. The chemical compositions were detected using the EDX with an accelerating voltage (15 kV). Additional information on element compositions was obtained using the Elemental analyzer (2400 Series II CHNS/O, PerkinElmer). For qualitative comparison, high-magnification images of the nanofibers and Pt NPs were obtained using a TEM (JEM-ARM 200F, JEOL) analysis at a high accelerating voltage of 200 kV. To investigate the structural evolution including crystal size and inter–d-spacing, XRD (Miniflex AD11605, Rigaku) was performed with Cu Kα source (λ = 1.5405 nm) at 30 mA, 30 kV, and room temperature. Data were collected from 10° to 90° on the scale of 2θ (2°/min). Furthermore, Raman spectroscopy (LabRam Aramis, Horriba) was used to determine the graphitization of the samples. The alteration of surface property and composition were examined using XPS with a monochromated Al x-ray source (K-alpha, Thermo U.K.). All binding energies were calibrated at C1s, 284.8 eV.

Electrochemical characterizations

The electrochemical properties of the developed electrode materials were characterized by the measurements of CV and LSV in 0.5 M H_2SO_4 (Sigma-Aldrich) at room temperature. These were used by applying to the Rotate Assembly Instructions (Pine Instruments) using a three-electrode system. A platinum wire was used as a counter electrode, and a standard calomel electrode [0.241 V versus reversible hydrogen electrode (RHE)] was used as a reference electrode. A mixture of ethanol (Sigma-Aldrich), Nafion solution (5 wt % in lower aliphatic alcohols and water; 1100 EW; Sigma-Aldrich), and samples were prepared as a catalyst slurry. For half-cell measurements, the slurry was deposited on a glassy carbon electrode (ϕ = 5 mm) and dried at room temperature in ambient air.

CVs were conducted between 0.05 and 1.2 V versus RHE with a rate of 50 mV/s in the N_2-saturated atmosphere. The ORR activity was investigated by recording the LSVs from 0.05 to 1 V_{RHE} at a rate of 20 mV/s with rotation at 1600 rpm in the O_2-saturated atmosphere. To evaluate the stability of the graphitized carbon supports, further investigations of electrochemical stability were performed using the following protocol based on the DOE and Fuel cell Commercialization Conference of Japan (FCCJ) durability test protocols: PCT for carbon corrosion test, 6000 cycles, 1.0 to 1.6 V, and scan rate 100 mV/s at 25°C (*15*).

This result of the cycling potential windows was adjusted on the basis of previous studies that used acceleration testing methods (*11*, *12*, *15*–*20*). The electrochemical alterations were recorded by following the CV and LSV methods after the PCTs. For comparison, commercial 40 wt % Pt/C (HISPEC 4000, Johnson Matthey) was used. After the PCTs, used catalysts were collected from the RDE by sonicating and then post-characterized by HR-TEM.

Single carbon web MEA for single-cell test

For fabricating the single-web MEAs, the synthesized Pt/PCA/CSW2500 was used for a cathode. First, for the anode, a catalyst slurry was prepared by mixing 40 wt % Pt/C commercial catalyst with DI water, Aquivion ionomer solution (D79-25BS), and isopropyl alcohol (Sigma-Aldrich) with an ionomer/carbon weight ratio of 25%. The slurries were stirred for 5 min and sonicated for 3 min, and these processes were repeated for 1 hour in ice-cold water. Subsequently, a CL was sprayed on the anode side of the Nafion HP (20 μm) with a Pt loading of 0.05 mg/cm^2 with sizes of 1 cm by 1 cm and 2.5 cm by 2.5 cm. To prepare a single-web cathode, the synthesized Pt/PCA/gCSW2500 was cut with sizes of

1 cm by 1 cm and 2.5 cm by 2.5 cm. Pt/PCA/gCSW2500 was then attached to the cathode side of the prepared membrane + Pt/C anode with a cathode Pt loading of 0.1 mg/cm^2. An ionomer solution of Aquivion 79-25BS diluted to 1% in isopropyl alcohol (IPA) was evenly impregnated drop by drop on the matrix of the single-web cathode to achieve an ionomer/carbon weight ratio of 5%. Then, the fabricated MEA was hot-pressed at 120°C at 0.3 ton/cm^2 for 3 min. Pt/gCSW2500 also was prepared following the same procedure. For a reference MEA, the commercial Pt/C catalyst was coated for the anode and cathode sides with Pt loading of 0.05 and 0.2 mg/cm^2, respectively. Last, a GDL (SGL 10BC) was used at both sides to facilitate the gas transfer, and then, single cells were assembled using the unit cell system with each end plate for PEMFC performance tests.

PEMFC performance and durability tests

The prepared MEAs were tested under the same conditions of 80°C and humidified condition of 50% RH using vaporized H_2O gas. The stoichiometry of the gas flows was 139/332 standard cubic centimeters per minute (SCCM) (H_2/air) with 1.8-atm absolute pressure. Before the tests, activation steps were applied to hydrate and stimulate the catalytic activity by applying 0.5 V for 20 hours. The polarization curves for *I-V* (current density–voltage) and *I-W* (current density–power density) were measured using a DC electrode load (6060B, Hewlett Packard). Electrochemical impedance spectroscopy (VSP with VMP3 booster or HCP-803 potentiostat, BioLogic) was applied to obtain information on the contact and interfacial resistances over a frequency range of 0.1 to 100,000 Hz. After fully purging N_2 gas in the cathode side, CV measurements were conducted to investigate the electrochemical properties.

For the durability comparison of the commercial Pt/C and Pt/PCA/gCSW2500 single web–based MEAs, two different protocols were carried out by the following conditions based on DOE (i) and NEDO (ii) durability test protocols (*17*, *21*).

Durability protocol (i) used the following: 1.0 to 1.5 V; scan rate, 500 mV/s at 80°C; RH100; and 20,000 cycles. The electrochemical changes were measured before and after every 500, 1000, 2000, 10,000, and 20,000 operation cycles using *I-V* and CV techniques. CV measurements were taken by flowing the gases through the electrode. The potential range was 0.05 to 1.2 V, and the scan rate was 50 mV/s.

Durability protocol (ii) used the following: 1.0 to 1.5 V; scan rate, 500 mV/s at 80°C; RH100; and 20,000 cycles. The electrochemical changes were measured before and after every 500, 1000, 2000, 10,000, and 20,000 operation cycles using *I-V* and CV techniques. CV measurements were taken after the N_2 gas flow through the cathode was stopped. The scan was done with the potential range of 0.05 to 0.9 V with a scan rate of 50 mV/s.

Supplementary Materials

This PDF file includes:

Figs. S1 to S14
Table S1 to S3

REFERENCES AND NOTES

1. H. A. Gasteiger, N. M. Marković, Just a dream—Or future reality? *Science* **324**, 48–49 (2009).
2. A. A. Franco, *Polymer Electrolyte Fuel Cells: Science, Applications and Challenges* (Pan Stanford Publishing, ed. 1, 2013).
3. M. Winter, R. J. Brodd, What are batteries, fuel cells, and supercapacitors? *Chem. Rev.* **104**, 4245–4270 (2004).
4. B. G. Pollet, S. S. Kocha, I. Staffell, Current status of automotive fuel cells for sustainable transport. *Curr. Opin. Electrochem.* **16**, 90–95 (2019).
5. B. D. James, J. M. Huya-Kouadio, C. Houchins, D. A. Desantis, Mass production cost estimation of direct H_2 PEM fuel cell systems for transportation applications: 2018 update (2018); www.sainc.com.
6. M. M. Whiston, I. L. Azevedo, S. Litster, K. S. Whitefoot, C. Samaras, J. F. Whitacre, Expert assessments of the cost and expected future performance of proton exchange membrane fuel cells for vehicles. *Proc. Natl. Acad. Sci. U.S.A.* **116**, 4899–4904 (2019).
7. M. K. Debe, Electrocatalyst approaches and challenges for automotive fuel cells. *Nature* **486**, 43–51 (2012).
8. Y. Wang, B. Seo, B. Wang, N. Zamel, K. Jiao, X. C. Adroher, Fundamentals, materials, and machine learning of polymer electrolyte membrane fuel cell technology. *Energy and AI* **1**, 100014 (2020).
9. L. Dubau, L. Castanheira, F. Maillard, M. Chatenet, O. Lottin, G. Maranzana, J. Dillet, A. Lamibrac, J. C. Perrin, E. Moukheiber, A. Elkaddouri, G. De Moor, C. Bas, L. Flandin, N. Caqué, A review of PEM fuel cell durability: Materials degradation, local heterogeneities of aging and possible mitigation strategies. *Wiley Interdiscip. Rev. Energy Environ.* **3**, 540–560 (2014).
10. M. Uchida, PEFC catalyst layers: Effect of support microstructure on both distributions of Pt and ionomer and cell performance and durability. *Curr. Opin. Electrochem.* **21**, 209–218 (2020).
11. K. H. Lim, H. S. Oh, S. E. Jang, Y. J. Ko, H. J. Kim, H. Kim, Effect of operating conditions on carbon corrosion in polymer electrolyte membrane fuel cells. *J. Power Sources* **193**, 575–579 (2009).
12. L. Castanheira, L. Dubau, M. Mermoux, G. Berthomé, N. Caqué, E. Rossinot, M. Chatenet, F. Maillard, Carbon corrosion in proton-exchange membrane fuel cells: From model experiments to real-life operation in membrane electrode assemblies. *ACS Catal.* **4**, 2258–2267 (2014).
13. F. Forouzandeh, X. Li, D. W. Banham, F. Feng, S. Ye, V. Birss, Understanding the corrosion resistance of meso- and micro-porous carbons for application in PEM fuel cells. *J. Electrochem. Soc.* **165**, F3230–F3240 (2018).
14. H. Yano, T. Akiyama, M. Watanabe, H. Uchida, High durability of Pt/graphitized carbon catalysts for polymer electrolyte fuel cells prepared by the nanocapsule method. *J. Electroanal. Chem.* **688**, 137–142 (2013).
15. A. Riese, D. Banham, S. Ye, X. Sun, Accelerated stress testing by rotating disk electrode for carbon corrosion in fuel cell catalyst supports. *J. Electrochem. Soc.* **162**, F783–F788 (2015).
16. N. Macauley, D. D. Papadias, J. Fairweather, D. Spernjak, D. Langlois, R. Ahluwalia, K. L. More, R. Mukundan, R. L. Borup, Carbon corrosion in PEM fuel cells and the development of accelerated stress tests. *J. Electrochem. Soc.* **165**, F3148–F3160 (2018).
17. Y. Hashimasa, Y. Matsuda, T. Shimizu, Comparison of carbon corrosion test methods for polymer electrolyte fuel cell. *Electrochim. Acta* **179**, 119–125 (2015).
18. Y. C. Park, K. Kakinuma, M. Uchida, H. Uchida, M. Watanabe, Deleterious effects of interim cyclic voltammetry on Pt/carbon black catalyst degradation during start-up/shutdown cycling evaluation. *Electrochim. Acta* **123**, 84–92 (2014).
19. J. H. Park, S. M. Hwang, G. G. Park, S. H. Park, E. D. Park, S. D. Yim, Variations in performance-degradation behavior of Pt/CNF and Pt/C MEAs for the same degree of carbon corrosion. *Electrochim. Acta* **260**, 674–683 (2018).
20. S. Park, Y. Shao, V. V. Viswanathan, J. Liu, Y. Wang, Non-kinetic losses caused by electrochemical carbon corrosion in PEM fuel cells. *Int. J. Hydrogen Energy* **37**, 8451–8458 (2012).
21. U. S. Drive Partnership., U. S. Driving Research and Innovation for Vehicle efficiency and Energy sustainability, U.S. DRIVE Fuel Cell Technical Team Roadmap (2017).
22. S. Sui, X. Wang, X. Zhou, Y. Su, S. Riffat, C.-j. Liu, A comprehensive review of Pt electrocatalysts for the oxygen reduction reaction: Nanostructure, activity, mechanism and carbon support in PEM fuel cells. *J. Mater. Chem. A* **5**, 1808–1825 (2017).
23. Y. Luo, N. Alonso-Vante, The effect of support on advanced Pt-based cathodes towards the oxygen reduction Reaction. State of the Art. *Electrochim. Acta* **179**, 108–118 (2015).
24. Z. Song, M. N. Banis, L. Zhang, B. Wang, L. Yang, D. Banham, Y. Zhao, J. Liang, M. Zheng, R. Li, S. Ye, X. Sun, Origin of achieving the enhanced activity and stability of Pt electrocatalysts with strong metal-support interactions via atomic layer deposition. *Nano Energy* **53**, 716–725 (2018).
25. A. Kumar, V. Ramani, Strong metal-support interactions enhance the activity and durability of platinum supported on tantalum-modified titanium dioxide electrocatalysts. *ACS Catal.* **4**, 1516–1525 (2014).
26. Y. Ji, Y. I. Cho, Y. Jeon, C. Lee, D. D.-H. Park, Y.-G. G. Shul, Design of active Pt on TiO_2 based nanofibrous cathode for superior PEMFC performance and durability at high temperature. *Appl. Catal. Environ.* **204**, 421–429 (2017).

27. Y. Jeon, Y. Ji, Y. I. Cho, C. Lee, D. H. Park, Y. G. Shul, Oxide-carbon nanofibrous composite support for a highly active and stable polymer electrolyte membrane fuel-cell catalyst. *ACS Nano* **12**, 6819–6829 (2018).
28. S. Murata, M. Imanishi, S. Hasegawa, R. Namba, Vertically aligned carbon nanotube electrodes for high current density operating proton exchange membrane fuel cells. *J. Power Sources* **253**, 104–113 (2014).
29. L. Ye, Y. Gao, S. Zhu, J. Zheng, P. Li, J. P. Zheng, A Pt content and pore structure gradient distributed catalyst layer to improve the PEMFC performance. *Int. J. Hydrogen Energy* **42**, 7241–7245 (2017).
30. D. Sebastián, A. G. Ruíz, I. Suelves, R. Moliner, M. J. Lázaro, V. Baglio, A. Stassi, A. S. Aricò, Enhanced oxygen reduction activity and durability of Pt catalysts supported on carbon nanofibers. *Appl. Catal. Environ.* **115-116**, 269–275 (2012).
31. S. Chan, J. Jankovic, D. Susac, M. S. Saha, M. Tam, H. Yang, F. Ko, Electrospun carbon nanofiber catalyst layers for polymer electrolyte membrane fuel cells: Structure and performance. *J. Power Sources* **392**, 239–250 (2018).
32. J. J. Slack, C. Gumeci, N. Dale, J. Parrondo, N. Macauley, R. Mukundan, D. Cullen, B. Sneed, K. More, P. N. Pintauro, Nanofiber fuel cell MEAs with a PtCo/C Cathodec. *J. Electrochem. Soc.* **166**, F3202–F3209 (2019).
33. N. Hodnik, L. Romano, P. Jovanovic, F. Ruiz-Zepeda, M. Bele, F. Fabbri, L. Persano, A. Camposeo, D. Pisignano, Assembly of Pt nanoparticles on graphitized carbon nanofibers as hierarchically structured electrodes. *ACS Appl. Nano Mater.* **3**, 9880–9888 (2020).
34. K. Waldrop, R. Wycisk, P. N. Pintauro, Application of electrospinning for the fabrication of proton-exchange membrane fuel cell electrodes. *Curr. Opin. Electrochem.* **21**, 257–264 (2020).
35. Y. Wang, Y. Pang, H. Xu, A. Martinez, K. S. Chen, PEM Fuel cell and electrolysis cell technologies and hydrogen infrastructure development - A review. *Energy Environ. Sci.* **15**, 2288–2328 (2022).
36. M. Uchida, Y. C. Park, K. Kakinuma, H. Yano, D. A. Tryk, T. Kamino, H. Uchida, M. Watanabe, Effect of the state of distribution of supported Pt nanoparticles on effective Pt utilization in polymer electrolyte fuel cells. *Phys. Chem. Chem. Phys.* **15**, 11236–11247 (2013).
37. C. Y. Ahn, J. E. Park, S. Kim, O. H. Kim, W. Hwang, M. Her, S. Y. Kang, S. Park, O. J. Kwon, H. S. Park, Y. H. Cho, Y. E. Sung, Differences in the electrochemical performance of Pt-based catalysts used for polymer electrolyte membrane fuel cells in liquid half- and full-cells. *Chem. Rev.* **121**, 15075–15140 (2021).
38. X. J. Cheng, C. Wang, G. H. Wei, X. H. Yan, S. Y. Shen, C. C. Ke, F. J. Zhu, J. L. Zhang, Insight into the effect of pore-forming on oxygen transport behavior in ultra-low Pt PEMFCs. *J. Electrochem. Soc.* **166**, F1055–F1061 (2019).
39. S. Guan, F. Zhou, J. Tan, M. Pan, Influence of pore size optimization in catalyst layer on the mechanism of oxygen transport resistance in PEMFCs. *Prog. Nat. Sci. Mater. Int.* **30**, 839–845 (2020).
40. T. Van Cleve, G. Wang, M. Mooney, C. F. Cetinbas, N. Kariuki, J. Park, A. Farghaly, D. Myers, K. C. Neyerlin, Tailoring electrode microstructure via ink content to enable improved rated power performance for platinum cobalt/high surface area carbon based polymer electrolyte fuel cells. *J. Power Sources* **482**, 228889 (2021).
41. F. Zhu, L. Luo, A. Wu, C. Wang, X. Cheng, S. Shen, C. Ke, H. Yang, J. Zhang, Improving the high-current-density performance of PEMFC through much enhanced utilization of platinum electrocatalysts on carbon. *ACS Appl. Mater. Interfaces* **12**, 26076–26083 (2020).
42. H. Ren, Y. Teng, X. Meng, D. Fang, H. Huang, J. Geng, Z. Shao, Ionomer network of catalyst layers for proton exchange membrane fuel cell. *J. Power Sources* **506**, 230186 (2021).
43. K. Fu, L. Zeng, J. Liu, M. Liu, S. Li, W. Guo, Y. Gao, M. Pan, Magnetron sputtering a high-performance catalyst for ultra-low-Pt loading PEMFCs. *J. Alloys Compd.* **815**, 152374 (2020).
44. M. S. Çögenli, S. Mukerjee, A. B. Yurtcan, Membrane electrode assembly with ultra low platinum loading for cathode electrode of PEM fuel cell by using sputter deposition. *Fuel Cells* **15**, 288–297 (2015).
45. O. H. Kim, Y. H. Cho, S. H. Kang, H. Y. Park, M. Kim, J. W. Lim, D. Y. Chung, M. J. Lee, H. Choe, Y. E. Sung, Ordered macroporous platinum electrode and enhanced mass transfer in fuel cells using inverse opal structure. *Nat. Commun.* **4**, 2473 (2013).
46. J. M. Kim, A. Jo, K. A. Lee, H. J. Han, Y. J. Kim, H. Y. Kim, G. R. Lee, M. Kim, Y. Park, Y. S. Kang, J. Jung, K. H. Chae, E. Lee, H. C. Ham, H. Ju, Y. S. Jung, J. Y. Kim, Conformation-modulated three-dimensional electrocatalysts for high-performance fuel cell electrodes. *Sci. Adv.* **7**, eabe9083 (2021).
47. M. S. A. Rahaman, A. F. Ismail, A. Mustafa, A review of heat treatment on polyacrylonitrile fiber. *Polym. Degrad. Stab.* **92**, 1421–1432 (2007).
48. H. Fujimoto, Theoretical X-ray scattering intensity of carbons with turbostratic stacking and AB stacking structures. *Carbon* **41**, 1585–1592 (2003).
49. S. C. Bennett, D. J. Johnson, Electron-microscope studies of structural heterogeneity in pan-based carbon fibres. *Carbon* **17**, 25–39 (1979).
50. A. Sadezky, H. Muckenhuber, H. Grothe, R. Niessner, U. Pöschl, Raman microspectroscopy of soot and related carbonaceous materials: Spectral analysis and structural information. *Carbon* **43**, 1731–1742 (2005).
51. M. Hara, M. Lee, C.-H. Liu, B.-H. Chen, Y. Yamashita, M. Uchida, H. Uchida, M. Watanabe, Electrochemical and Raman spectroscopic evaluation of Pt/graphitized carbon black catalyst durability for the start/stop operating condition of polymer electrolyte fuel cells. *Electrochim. Acta* **70**, 171–181 (2012).
52. K. Shinozaki, Y. Morimoto, B. S. Pivovar, S. S. Kocha, Re-examination of the Pt particle size effect on the oxygen reduction reaction for ultrathin uniform Pt/C catalyst layers without influence from nafion. *Electrochim. Acta* **213**, 783–790 (2016).
53. M. Shao, A. Peles, K. Shoemaker, Electrocatalysis on platinum nanoparticles: Particle size effect on oxygen reduction reaction activity. *Nano Lett.* **11**, 3714–3719 (2011).
54. M. Nesselberger, S. Ashton, J. C. Meier, I. Katsounaros, K. J. J. Mayrhofer, M. Arenz, The particle size effect on the oxygen reduction reaction activity of Pt catalysts: Influence of electrolyte and relation to single crystal models. *J. Am. Chem. Soc.* **133**, 17428–17433 (2011).
55. M. Inaba, A. Zana, J. Quinson, F. Bizzotto, C. Dosche, A. Dworzak, M. Oezaslan, S. B. Simonsen, L. T. Kuhn, M. Arenz, The oxygen reduction reaction on Pt: Why particle size and interparticle distance matter. *ACS Catal.* **11**, 7144–7153 (2021).
56. G. Shi, T. Tano, D. A. Tryk, A. Iiyama, M. Uchida, K. Kakinuma, Temperature dependence of oxygen reduction activity at Pt/Nb-doped SnO2 catalysts with varied Pt loading. *ACS Catal.* **11**, 5222–5230 (2021).
57. M. Li, Z. Zhao, T. Cheng, A. Fortunelli, C. Y. Chen, R. Yu, Q. Zhang, L. Gu, B. V. Merinov, Z. Lin, E. Zhu, T. Yu, Q. Jia, J. Guo, L. Zhang, W. A. Goddard, Y. Huang, X. Duan, Ultrafine jagged platinum nanowires enable ultrahigh mass activity for the oxygen reduction reaction. *Science* **354**, 1414–1419 (2016).
58. D. J. S. Sandbeck, N. M. Secher, M. Inaba, J. Quinson, J. E. Sørensen, J. Kibsgaard, A. Zana, F. Bizzotto, F. D. Speck, M. T. Y. Paul, A. Dworzak, C. Dosche, M. Oezaslan, I. Chorkendorff, M. Arenz, S. Cherevko, The dissolution dilemma for low Pt loading polymer electrolyte membrane fuel cell catalysts. *J. Electrochem. Soc.* **167**, 164501 (2020).
59. D. L. Wood, R. L. Borup, Estimation of mass-transport overpotentials during long-term PEMFC operation. *J. Electrochem. Soc.* **157**, B1251–B1251 (2010).
60. B. Li, M. Xie, K. Wan, X. Wang, D. Yang, Z. Liu, T. Chu, P. Ming, C. Zhang, A high-durability graphitic black pearl supported Pt catalyst for a proton exchange membrane fuel cell stack. *Membranes* **12**, (2022).
61. M. Wu, Q. Wang, K. Li, Y. Wu, H. Liu, Optimization of stabilization conditions for electrospun polyacrylonitrile nanofibers. *Polym. Degrad. Stab.* **97**, 1511–1519 (2012).
62. J. Parrondo, T. Han, E. Niangar, C. Wang, N. Dale, K. Adjemian, V. Ramani, Platinum supported on titanium-ruthenium oxide is a remarkably stable electrocatayst for hydrogen fuel cell vehicles. *Proc. Natl. Acad. Sci. U.S.A.* **111**, 45–50 (2014).
63. J. P. Owejan, J. E. Owejan, W. Gu, Impact of platinum loading and catalyst layer structure on PEMFC performance. *J. Electrochem. Soc.* **160**, F824–F833 (2013).
64. S. Liu, S. Li, R. Wang, Y. Rao, Q. Zhong, K. Hong, M. Pan, Preparation of high performance and ultra-low platinum loading membrane electrode assembly for PEMFC commercial application. *J. Electrochem. Soc.* **166**, F1308–F1313 (2019).
65. Q. Cheng, S. Yang, C. Fu, L. Zou, Z. Zou, Z. Jiang, J. Zhang, H. Yang, High-loaded sub-6 nm Pt1Co1 intermetallic compounds with highly efficient performance expression in PEMFCs. *Energy. Environ. Sci.* **15**, 278–286 (2022).
66. X. Duan, F. Cao, R. Ding, X. Li, Q. Li, R. Aisha, S. Zhang, K. Hua, Z. Rui, Y. Wu, J. Li, A. Li, J. Liu, Cobalt-doping stabilized active and durable sub-2 nm Pt nanoclusters for low-Pt-loading PEMFC cathode. *Adv. Energy Mater.* **12**, 2103144 (2022).
67. L. Chong, J. Wen, J. Kubal, F. G. Sen, J. Zou, J. Greeley, M. Chan, H. Barkholtz, W. Ding, D.-J. Liu, Ultralow-loading platinum-cobalt fuel cell catalysts derived from imidazolate frameworks. *Science* **362**, 1276–1281 (2018).
68. J. S. Spendelow, Advanced electro-catalysts through crystallographic enhancement. DOE Annual Merit Review (2019).
69. Y. Chino, K. Taniguchi, Y. Senoo, K. Kakinuma, M. Hara, M. Watanabe, M. Uchida, Effect of added graphitized CB on both performance and durability of Pt/Nb-SnO_2 cathodes for PEFCs. *J. Electrochem. Soc.* **162**, F736–F743 (2015).
70. Z. Qiao, S. Hwang, X. Li, C. Wang, W. Samarakoon, S. Karakalos, D. Li, M. Chen, Y. He, M. Wang, Z. Liu, G. Wang, H. Zhou, Z. Feng, D. Su, J. S. Spendelow, G. Wu, 3D porous graphitic nanocarbon for enhancing the performance and durability of Pt catalysts: A balance between graphitization and hierarchical porosity. *Energy. Environ. Sci.* **12**, 2830–2841 (2019).

Acknowledgments

Funding: This research was supported by National Nuclear R&D Program through the NRF funded by the Ministry of Science and ICT (NRF-2020M2D8A2064728) and KIURI Korea Initiative for fostering University of Research and Innovation Program of NRF (2020M3H1A1077207) and

also by "Regional Innovation Strategy (RIS)" through the National Research Foundation of Korea (NRF) funded by the Ministry of Education (MOE) (2022RIS-005). **Author contributions:** Y.Ji: conceptualization, methodology, validation, and writing (original draft). O.K.: formal analysis and methodology. O.S.J.: formal analysis and methodology. S.Y.: investigation and validation. Y.Jeon: investigation, data curation, and writing (original draft). Y.Shul: validation, supervision, and resources. All authors have given approval to the final version of the manuscript.
Competing interests: The authors declare that they have no competing interests. **Data and materials availability:** All data needed to evaluate the conclusions in the paper are present in the paper and/or the Supplementary Materials.

Submitted 25 October 2022
Accepted 24 March 2023
Published 28 April 2023
10.1126/sciadv.adf4863